Research Square

Preprints are preliminary reports that have not undergone peer review.
They should not be considered conclusive, used to inform clinical practice,
or referenced by the media as validated information.

ADGRG1 blockade drives astrocytes into the extracellular matrix to reduce glial scar size

Gentaro Ono
Kyushu University
Kazu Kobayakawa
kobayakawa.kazu.000@m.kyushu-u.ac.jp

Kyushu University
Hirokazu Saiwai
Spinal Injuries Center
Kazuya Yokota
Kyushu University
Tetuya Tamaru
Kyushu University
Kazuhiro Hata
Spinal Injuries Center
Hirotaka Iura
Kyushu University
Yohei Haruta
Kyushu University
Kazuki Kitade
Kyushu University
Jun Kishikawa
Kyushu University
Kiyoshi Tarukado
Kyushu University
Kenichi Kawaguchi
Kyushu University
Dai-Jiro Konno
Kindai University
Kinichi Nakashima
Kyushu University
Takeshi Maeda
Spinal Injuries Center
Seiji Okada

Osaka University

Yasuharu Nakashima

Kyushu University

Research Article

Keywords: spinal cord injury, glial scar, type III collagen, ADGRG1, astrocyte, RhoA

Posted Date: August 12th, 2026

DOI: https://doi.org/10.21203/rs.3.rs-10546825/v1

License: This work is licensed under a Creative Commons Attribution 4.0 International License.
Read Full License

Additional Declarations: No competing interests reported.

Abstract

Background

After wide range of traumatic damage to the spinal cord, reactive astrocytes migrate toward the lesion but stop at the edge of the fibrotic extracellular matrix (ECM) core. There, the reactive astrocytes accumulate and form the glial scar border that prevents the regenerating axons from passing through. Why these astrocytes stop at this border rather than entering the ECM remains unknown. We reasoned that this stop signal comes from the fibrotic ECM. Among its components, we focused on type III collagen, which is abundant in the core but whose role in scar formation is unknown.

Methods

We analyzed single-nucleus RNA-sequencing and spatial transcriptomic datasets of mouse spinal cords. Using cell-cell interaction analysis, we searched for the astrocyte receptor that binds type III collagen. We then tested the candidate pathway in primary astrocytes *in vitro*, *in vivo* using pharmacological and genetic inhibition, and in human induced pluripotent stem cell (hiPSC)-derived astrocytes.

Results

We found six astrocyte subclusters that changed over time. Among them, reactive astrocytes showed a strong interaction between type III collagen, encoded by *Col3a1*, and adhesion G protein-coupled receptor G1 (ADGRG1). *Col3a1*-expressing vascular leptomeningeal cells (VLMCs) and arachnoid barrier cells (ABCs) sat next to ADGRG1-expressing astrocytes at the fibrotic border. *In vitro*, type III collagen activated RhoA-GTP loading through ADGRG1 and suppressed astrocyte migration. This effect was specific to type III collagen and was reversed by the ADGRG1 antagonist Dihydromunduletone (DHM). *In vivo*, both pharmacological inhibition of ADGRG1 and astrocyte-specific *Adgrg1* knockdown let astrocytes enter the type III collagen-rich matrix. This produced smaller glial scars, enhanced corticospinal tract (CST) regeneration, and improved motor recovery. The same response occurred in hiPSC-derived astrocytes.

Conclusions

Type III collagen keeps astrocytes at the edge of the fibrotic ECM and stops them from entering it, acting through ADGRG1–RhoA signaling. This sets the position of the glial scar border. The type III collagen–ADGRG1 axis may be a new therapeutic target for controlling maladaptive scarring after CNS injury.

Background

Central nervous system (CNS) injury, including spinal cord injury (SCI), produces a lesion with a distinct bilayered structure. At the lesion core lies a fibrotic extracellular matrix (ECM). This core is surrounded by a dense layer of reactive astrocytes that strongly express glial fibrillary acidic protein (GFAP) and form the glial scar border [1, 2]. This border forms within days of injury, persists into the chronic phase, and is

a structural hallmark of CNS scarring. Reactive astrogliosis at this border initially serves protective functions, limiting lesion expansion and facilitating blood–spinal cord barrier repair, but it also creates physical and biochemical barriers to axonal regrowth [3, 4]. This bilayered structure forms after injury: fibrotic ECM is deposited around the lesion epicenter, and reactive astrocytes migrate toward the lesion and settle around this ECM. The astrocytes stop at the edge of the fibrotic ECM core instead of entering it. How astrocytes are stopped at this border and which receptor detects the stop signal remain key unanswered questions in the CNS.

We reasoned that the signal stopping astrocytes at this border come from the ECM of the fibrotic core. Chondroitin sulfate proteoglycans secreted by reactive astrocytes are well-established axonal growth inhibitors [5]. More recently, fibrotic ECM components such as collagens have also been shown to actively regulate glial cell behavior. Type I collagen promotes astrocytic scar formation through the integrin–N-cadherin pathway[5]. Type III collagen is similarly deposited abundantly in the lesion core following SCI with upregulated expression[5, 6]. However, the functional role of type III collagen in scar architecture remains poorly understood.

Type III collagen is a known ligand for adhesion G protein-coupled receptor G1 (ADGRG1), also known as GPR56. ADGRG1 belongs to the adhesion G protein-coupled receptor (GPCR) family and is characterized by an extensive N-terminal extracellular region containing a pentraxin/laminin-neurexin-sex-hormone-binding-globulin-like (PLL) domain and a GPCR autoproteolysis-inducing domain [7–9]. Type III collagen binds to the PLL domain and activates RhoA signaling through Gα12/13 coupling [10, 11]. In the developing cerebral cortex, this type III collagen–ADGRG1 pathway stops neuronal migration [10]. ADGRG1 also mediates diverse functions, including CNS myelination and microglia-mediated synaptic pruning [12–14]. However, whether ADGRG1 mediates a similar response in astrocytes, particularly after CNS injury, is unknown.

In this study, we asked what stops migrating astrocytes at the edge of the fibrotic ECM and thereby builds the bilayered scar. Using single-nucleus RNA-sequencing and spatial transcriptomics of mouse spinal cords before and at 1, 4, 7, 14, and 30 days after injury, together with validation in human induced pluripotent stem cell-derived astrocytes, we identify type III collagen as a key regulator of astrocyte positioning during scar formation. Type III collagen activates ADGRG1 and its downstream effector RhoA, which keeps astrocytes at the edge of the fibrotic ECM and stops them from entering it. Genetic or pharmacological inhibition of this pathway lets astrocytes enter the fibrotic ECM, leading to smaller glial scars, enhanced axonal regeneration, and improved motor recovery. These findings identify the type III collagen–ADGRG1 axis as a previously unrecognized signal that positions astrocytes during CNS scar formation and may open new avenues for therapies that modulate scar pathology after CNS injury.

Materials and methods

Animals

All mice were housed in a temperature- and humidity-controlled environment with a 12-hour light-dark cycle and ad libitum access to food and water. Eight-week-old C57BL/6 mice were used for in vivo spinal cord injury experiments, with equal numbers of males and females allocated to each experimental cohort (cohort sizes are reported in the corresponding figure legends). C57BL/6 mice at postnatal day 2 were used for primary astrocyte cultures; sex was not determined at this age because reliable sex identification is not feasible in neonates. For astrocyte isolation by flow cytometry, eight-week-old Aldh1l1-EGFP mice (3 males and 2 females) and age-matched C57BL/6 control mice (3 males and 2 females) were used; the sex ratio was matched between the two genotypes to ensure direct comparability. In total, 82 mice were used in this study: 64 C57BL/6 mice for in vivo SCI experiments, 5 C57BL/6 mice as controls for flow cytometry, 5 Aldh1l1-EGFP mice for flow cytometry, and 8 neonatal C57BL/6 pups for primary astrocyte cultures. Sample sizes were determined based on previous studies using the same SCI model.

Spinal cord injury

The mice were anesthetized with 2% isoflurane and subjected to contusion injury (70 kilodynes) at the 10th thoracic level using an Infinite Horizons Impactor (Precision Systems Instrumentation) [15]. After the injury, the overlying muscles were sutured in layers, and the skin was closed with wound clips. Body temperature and hemodynamic status were monitored during recovery from anesthesia, and animals were confirmed to be mobile without signs of distress before being returned to their home cages. Manual bladder expression was performed twice daily until spontaneous voiding was re-established. Animals were monitored daily for signs of distress, including self-mutilation, abnormal posture, and tachypnea. If such signs were observed, meloxicam (0.2 mg/kg, subcutaneously, once daily) was administered for analgesia. In cases of suspected wound infection, evidenced by discharge from the surgical site, tetracycline (10 mg/kg/day, subcutaneously) was administered. Humane endpoints included persistent infection unresponsive to antibiotic treatment for more than one week or continuous bleeding for more than three days post-surgery, at which point animals were euthanized by cervical dislocation under deep isoflurane anesthesia.

Drug and AAV injection into the spinal cord

Dihydromunduletone (DHM; HY-101483; MCE) was dissolved in dimethyl sulfoxide (DMSO) to prepare a 10 mM stock solution [16]. For cell culture experiments, the stock solution was diluted with culture medium to the desired concentration. For animal administration experiments, it was diluted in PBS to the appropriate concentration (100μM) and used as directed. The following AAVs were used: control AAV (AAV2/1-CMV-EGFP; 1 × 10^{13} vg/mL; VB010000-9397wgw; VectorBuilder), an *Adgrg1* knockdown vector (AAV2/1-GFAP-sh*Adgrg1*-EGFP; 1 × 10^{13} vg/mL; VB220407-1443ruj; VectorBuilder), and AAV2/1-CAG-tdTomato (1 × 10^{13} vg/mL; 59462; Addgene). For *Adgrg1* knockdown and control AAV experiments, 2 μL of AAV was injected into the spinal cord parenchyma. Injections were delivered at 0.5 μL/min through a glass micropipette using a syringe pump (KDS 310; Muromachi Kikai) mounted on a stereotaxic frame.

Primary astrocyte cultures

Purified primary astrocyte cultures were prepared from C57BL/6 mice, as previously described [17, 18]. In brief, after removal of the meninges, on postnatal day 2, mouse brain tissues were minced and incubated in a water bath at 37°C for 30 min in DMEM (08456-36; Nacalai Tesque) in the presence of 0.25% trypsin (35554-64; Nacalai Tesque) and 300 μg/ml DNase I (Sigma-Aldrich). Dissociated cells were triturated with 0.25% fetal bovine serum (FBS) and centrifuged at 300 ×*g* for 3 min. Following dilution with astrocyte-specific medium (DMEM containing 10% FBS and 1% penicillin-streptomycin), the cells were plated on a poly-L-lysine-coated T75 flask. After 7 days in a humidified CO_2 incubator at 37°C, the T75 flask was set up on an orbital shaker to remove microglia at 180 rpm for 30 minutes. Fresh astrocyte culture medium (20 mL) was added, and the flask was shaken at 240 rpm for 6 hours to remove the oligodendrocyte precursor cells. Astrocytes were detached from T75 flasks using 0.25% trypsin. Astrocytes were stimulated with 50 ng/ml IL-6 (R&D Systems) and 200 ng/ml soluble IL-6 receptor (R&D Systems) for one day. Regular mycoplasma testing was performed, and all results were negative throughout the course of the present experiments. Testing was performed using MycoStrip (rep-mys-10; INVIVOG). These experiments were performed using cells derived from independent culture preparations. Within each experiment, treatment groups were assigned to wells in a randomized plate layout to minimize positional effects. Each well was automatically assigned a randomized, anonymous identifier prior to imaging and quantification. Group allocation was revealed and matched to the dataset only after all measurements were completed, ensuring blinded outcome assessment.

hiPSC-derived astrocytes cultures

We used human induced pluripotent stem cell (hiPSC)-derived cells purchased from Elixirgen Scientific (AS-SeV-CW50065; Elixirgen Scientific). The cells were cultured for 14 days, as specified by the kit, and used for the experiments. These experiments were performed using cells derived from independent culture preparations. Within each experiment, treatment groups were assigned to wells in a randomized plate layout to minimize positional effects. Each well was automatically assigned a randomized, anonymous identifier prior to imaging and quantification. Group allocation was revealed and matched to the dataset only after all measurements were completed, ensuring blinded outcome assessment.

Collagen coating

Collagen-coated dishes were prepared according to a modified protocol from the manufacturer (Nippi, Tokyo). Type III collagen (PSC-3-100-05; Nippi) stock solution was diluted with 5 mM acetic acid to a final concentration of 8.0 μg/mL. The 5 mM acetic acid solution was prepared by adding 4 μL of acetic acid to 14 mL of MilliQ water and sterilized by filtration through a 0.22 μm filter. The diluted collagen solution (500 μL) was added to each well of a 24-well plate, incubated at room temperature for 30 minutes, washed with PBS, and used immediately for cell culture. Type I collagen (1066; Chondrex), type III collagen (custom order; Chondrex), and type IV collagen (3410-010-02; R&D Systems) used in the cell

migration assay were coated by the same procedure. Each collagen was diluted in 5 mM acetic acid to the same final concentration of 8.0 μg/mL, and 100 μL of the diluted solution was added to each well of the Oris Cell Migration Assembly Kit-FLEX.

Scratch assay

Mouse astrocytes were plated on poly-L-lysine (P1399; Sigma-Aldrich)- coated or type III collagen-coated surfaces. After reaching sub-confluence, we treated cells with 10 μg/mL mitomycin C (20898-21; Nacalai Tesque) for 2 hours to prevent cell proliferation, then scratched them. Similarly, hiPSC-derived astrocytes were plated on coverslips coated with Geltrex (A1569601; Thermo Fisher Scientific) or type III collagen. A cell-free area was then created by scratching the monolayer with a 200 μL pipette tip. For DHM-treated groups, DHM was added to the culture medium immediately before scratching at a final concentration of 20 μM; vehicle controls received an equivalent volume of DMSO. Cells were allowed to migrate into the cell-free area for 48 hours. At 48 hours post-scratch, five (mouse astrocytes) or six (hiPSC-derived astrocytes) non-overlapping fields per well were imaged, and the number of astrocytes that had migrated into the cell-free area was quantified as described previously [18].

Single-cell tracking assay

Mouse astrocytes were seeded at a low density (approximately 30% confluency) with poly-L-lysine or type III collagen. For hiPSC-derived astrocytes, cells were plated at low density on coverslips coated with Geltrex or type III collagen. To assess dynamic astrocyte behavior, time-lapse imaging was performed under a phase-contrast microscope equipped with a temperature- and CO_2-controlled incubator. Images of six (mouse astrocytes) or ten (hiPSC-derived astrocytes) astrocytes per condition were acquired every 10 minutes for a total of 6 hours. For the DHM-treated group, DHM was added to the culture medium at a final concentration of 20 μM prior to initiating time-lapse imaging. The resulting image sequences were analyzed to track individual astrocyte migration and quantify morphological changes using ImageJ (NIH). Key parameters included cell migration distance, speed, and process length.

Cell migration assay

Cells (5×10^4 cells per well) were seeded into wells of the Oris Cell Migration Assembly Kit-FLEX (CMAUFL4; PlatypusTechnologies), coating with type I collagen (1066; Chondrex), type III collagen (custom order; Chondrex), or type IV collagen (3410-010-02; R&D Systems). Migration assays were conducted in accordance with the manufacturer's instructions. After 16 hours of attachment, cells were allowed to migrate into the clear field after removal of the well inserts. Cells were then fixed with 4% PFA and stained with primary antibodies against GFAP. Nuclear counterstaining was performed using Hoechst 33342. The images were analyzed using ImageJ.

Immunohistochemistry (IHC)

Mice were anesthetized and transcardially perfused with normal saline, followed by 4% paraformaldehyde (PFA) in 0.1 M phosphate-buffered saline. The spinal cord was removed and immersed in 4% PFA at 4°C for 24 hours. A spinal segment centered over the lesion epicenter was transferred into 10% sucrose in PBS for 24 hours and 30% sucrose in PBS for 24 hours and embedded in optimal cutting temperature compound. The embedded tissue was immediately frozen in liquid nitrogen and stored at -80°C until use. Frozen sections were cut with a cryostat in the sagittal or axial plane at 16 μm and mounted onto glass slides as previously described [19]. For immunofluorescence staining, the spinal cord sections were permeabilized with 0.01% Triton X-100 and 10% normal goat serum in PBS (pH 7.4) for 60 minutes. The sections were then stained with primary antibodies against GFAP (1:500; astrocyte marker, rat; 13–0300; Invitrogen), Type III collagen (1:500; rabbit; 22734-1-AP; Protein Tech), or ADGRG1 (1:500; rabbit; bs-11848R; Bioss). The sections were then incubated with Alexa Fluor-conjugated secondary antibodies (1:1000; Invitrogen). Nuclear counterstaining was performed using Hoechst 33342 (1:1000; Invitrogen). All images were captured using a BZ-X700 digital microscope system (Keyence) or epifluorescence microscope equipped with a digital camera (BX51; Olympus). Scar volume was quantitatively evaluated by measuring the scar area in every serial section taken at 80 μm intervals and approximating the scar volume. For quantification of the GFAP-positive area inside type III collagen, the section showing the maximum scar area was used, and the GFAP-positive area within the region of dense type III collagen staining was measured. All measurements were performed using ImageJ.

RhoA activity assay

RhoA activity was measured using the RhoA G-LISA Activation Assay Kit (BK124, Cytoskeleton, Denver, CO) according to the manufacturer's protocol. Cultured astrocytes were harvested in ice-cold lysis buffer, and cell lysates were centrifuged at 10,000 × g for 2 minutes at 4°C to obtain supernatants. Protein concentration was determined using the Precision Red protein assay reagent provided with the kit, and samples were adjusted to equal concentrations. Adjusted lysates were added to 96-well plates coated with RhoA-GTP binding protein and incubated at 4°C for 30 minutes on an orbital shaker (400 rpm). After washing, an anti-RhoA primary antibody was added and incubated at room temperature for 45 minutes, followed by incubation with HRP-conjugated secondary antibody at room temperature for 45 minutes. HRP detection reagent was added, and after color development, HRP stop solution was added. Absorbance at 490 nm was measured using a microplate reader.

Reverse transcription quantitative real-time PCR (RT-qPCR)

Total RNA was isolated from astrocytes and spinal cord tissues using a RNeasy Mini Kit (74104; Qiagen). cDNA was synthesized from total RNA using PrimeScript Reverse Transcriptase (2680; Takara), according to the manufacturer's instructions. RT-qPCR was performed using primers specific to the genes of interest and SYBR Premix Dimer Eraser (RR091A; Takara). The data were normalized to glyceraldehyde-3-phosphate dehydrogenase (GAPDH) levels. RT-qPCR was performed using a CFX

Connect Real-Time PCR Detection System (Bio-Rad). Using one cDNA sample, we examined the mRNA expression of the various factors listed in Supplementary Table 1.

Analyses of the locomotor function

The motor function of the paralyzed hind paws was evaluated using a locomotor open-field rating scale on the Basso Mouse Scale (BMS) and a footprint analysis. For BMS, each mouse was assessed at 1, 4, 7, 14, 21, 28, 35, and 42 days post-injury (dpi). A team of three independent examiners evaluated each animal for 4 minutes and assigned a BMS score. The median score of the three examiners was used for analysis. For footprint analysis, the forepaws and hindpaws were painted with red and green ink, respectively, and mice were allowed to walk along a paper-lined corridor, as previously described [20]. All tests were performed in a double-blinded manner as previously described [15].

Neuronal tracing

At 14 dpi, a craniotomy was performed to expose the sensorimotor cortex. tdTomato-encoding AAV was injected into the hemisphere. Eight mice per group received AAV-*Cag-tdTomato*. For the mouse, three injections for cortex (AAVs; 1.0×10^{13} virus genome/mL, 1 μL per site) were performed at the following coordinates: 1.0 mm lateral, 1.0 mm depth; and − 1.0 mm, 0 mm, 1.0 mm posterior to the bregma. Six weeks post-SCI (4 weeks post-AAV injection), the spinal cord was fixed with PFA, as described above. Sections were taken on the caudal and rostral sides (1.5 mm) from the center of the injury to assess how tdTomato-positive areas projected to the caudal side in comparison to sections on the rostral side [21].

Three-dimensional reconstruction of immunostaining

Spinal cord sequential sections at 80-μm intervals were stained with antibodies against GFAP and type III collagen; type III collagen-positive areas surrounded by strongly GFAP-positive areas were defined as scar and non-scar tissue was removed. Stacked images were created by positioning the images with markers. The stacked images were converted to 3D data using the ImageJ software program.

Flow cytometry

Spinal cords (4.0 mm in length, centered around the lesion) were dissociated using collagenase type I (17100017; Invitrogen), as previously described [22]. The ALDH1L1-positive cells or AAV-infected astrocytes were sorted as EGFP-positive cells using a FACSAria Fusion Flow Cytometer and the FACSDiva software program (BD Biosciences).

Single nuclear RNA sequencing (snRNA-seq) analysis

We analyzed public snRNA-seq datasets [23] with Scanpy v.1.7.0 [24], with the pipeline following their documentation. Specifically, clustering was performed using the Leiden algorithm. Gene expression values were scaled, and principal component analysis (PCA) was performed using the top 30 components. A *k*-nearest neighbor graph was constructed (n_neighbors = 30, n_pcs = 30) and used to compute Uniform Manifold Approximation and Projection (UMAP) embeddings and Partition-based Graph Abstraction (PAGA) trajectories, with clusters defined by the simplified Leiden annotation. Cell

annotation was performed with CellTypist with modified name for spinal cord tissue [25–27]. Cell interaction analysis was performed using CellPhoneDB v5.0 [28], with the pipeline after translating with mouse-to-human gene symbol conversion using mousipy. To account for the proportional contribution of each astrocyte subtype across timepoints, interaction scores were weighted by the relative proportion of each astrocyte subtype among total astrocytes at each timepoint. Cell proportions were computed from the full integrated dataset by aggregating cell counts per subtype and time point. Weighted interaction scores (interaction score × receiver cell proportion) were summarized using stacked area plots, displayed separately for each sender cell type (VLMC_1, ABC_1, ABC_2), to visualize the temporal dynamics of type III collagen–ADGRG1 signaling directed at individual astrocyte subclusters.

Spatial transcriptomics

We analyzed public spatial transcriptomics datasets [23] using Scanpy v.1.7.0 [24]. As a reference, we utilized the snRNA-seq dataset and performed supervised label transfer to map predicted cell type annotations onto the spatial transcriptomics data. Specifically, cell types identified in the snRNA-seq data were transferred to the spatial transcriptomics dataset by matching shared marker gene expression profiles and predicted labels. We then integrated the normalized gene expression matrices with spatial coordinates to construct 3D spatial representations. To explore local spatial interactions, we applied K-nearest neighbor classification (n = 5) to the coordinate data, identifying adjacent cells and calculating the average expression of target genes in their neighborhood. We selectively visualized astrocytes near *Col3a1*-expressing cells using matplotlib, highlighting the spatial distribution and microenvironmental interactions of the annotated cell types.

Statistical analysis

All statistical analyses were performed using GraphPad Prism 10 version 10.0.3 (GraphPad Software Inc.) following the suggested test parameters. Details regarding the statistical analysis of experiments throughout the study can be found in the figure legends. For all parametric analyses, approximate normality was assumed based on prior studies using the same experimental model. For one-way ANOVA and unpaired t-tests, homogeneity of variance was assessed using the Brown–Forsythe test. For two-way repeated-measures ANOVA, sphericity was assumed; where this assumption may not hold, Greenhouse–Geisser correction was applied.

Results

Temporal dynamics of astrocyte subclusters after SCI

To investigate how astrocytes respond to SCI over time, we analyzed publicly available single-nucleus RNA-sequencing (snRNA-seq) datasets of spinal cord tissue from uninjured mice and mice at multiple time points post-injury [23]. Using unsupervised clustering and CellTypist-based cell type annotation of spinal cord samples obtained at pre-injury and 1, 4, 7, 14 days and 1-month post-injury, we identified 59 distinct cellular clusters, including several astrocyte populations (Fig. 1a, Supplementary Fig. 1) [25–27].

snRNA-seq analysis identified six astrocyte subclusters (Astro_1–6) with distinct temporal dynamics and molecular profiles (Fig. 1b, c). In the uninjured spinal cord, Astro_3 was dominant, showing strong homeostatic (*Aqp4*, *Kcnj10*)[29, 30] and low inflammatory gene expression (*C3*, *Lcn2*, *Serpina3n*) [31–33]. After the injury, the subclusters changed over time. At 1 dpi, two transient subclusters emerged, Astro_2 and Astro_4. Astro_4 showed the highest expression of *Nes* [5], *Mt1*[34], and *S100a10*[32], genes known to be upregulated during the acute phase of injury, while partially retaining homeostatic markers (Fig. 1b). Astro_2 showed a pronounced loss of the homeostatic marker *Kcnj10* but still expressed reactive markers at low levels, suggesting an early departure from homeostasis. At 4 dpi, Astro_6 predominated, showing maximal *Vim* and strong *Gfap* expression alongside the lowest *Lcn2* among the early-reactive subclusters (Astro_2, Astro_4, and Astro_6). From 7 dpi onward, Astro_5 became dominant and persisted into the chronic phase, expressing the highest *Id3* together with elevated *Sox9*, *C3*, *Xylt1*, and *Serpina3n*, markers of reactive astrogliosis and glial scar formation [5, 35]. Astro_1 was a subacute-to-chronic population with intermediate expression of both homeostatic and inflammatory markers, reflecting incomplete resolution of the injury response. Notably, Astro_5 was also detected at a low proportion in the uninjured spinal cord, consistent with recent single-cell studies reporting reactive-like astrocyte subpopulations in the naive CNS [35, 36]. This temporal order was supported by the connectivity between subclusters assessed by PAGA (Fig. 1d). Astro_2 retained connectivity with the homeostatic Astro_3, whereas Astro_4 connected to Astro_3 only indirectly, through Astro_2 and Astro_6. This is consistent with Astro_2 being an early transitional state that stays linked to the normal state while branching towards the acute-phase Astro_4 and Astro_6 states. Together, these results indicate that astrocytes dynamically change their gene-expression phenotype after SCI.

Role of type III collagen in astrocyte behavior

To clarify how type III collagen, encoded by *Col3a1*, affects astrocytes, we performed pathway analysis using CellPhoneDB with snRNA-seq data [28]. Among the various type III collagen-associated pathways, the ADGRG1-mediated pathway exhibited strong interactions with multiple astrocyte subtypes (Fig. 2a-b). Because astrocyte subtype composition changes substantially over time, we adjusted the interaction scores according to the proportion of each subtype at each time point. This analysis revealed that the type III collagen-ADGRG1 pathway score decreased during the hyperacute phase, recovered between 1 and 7 dpi, and thereafter remained at a sustained plateau (Fig. 2c). Furthermore, spatial transcriptomic analysis demonstrated that Astro_1, 3 and 5 localize in proximity to cells strongly expressing *Col3a1*, particularly those belonging to the vascular leptomeningeal cell (VLMC) _1 and arachnoid barrier cell (ABC)_1 and _2 clusters (Fig. 2d, Supplementary Fig. 2). These snRNA-seq and spatial transcriptomic analyses indicated that the type III collagen-ADGRG1 pathway dynamically regulates astrocyte behavior in the local microenvironment of the injured spinal cord.

ADGRG1 inhibition enables astrocytes to enter the fibrotic ECM

We next investigated whether blocking the ADGRG1 pathway could change the structure of the glial scar *in vivo*. We first injected the ADGRG1 antagonist, dihydromunduletone (DHM), directly into the injured spinal cord [16]. Based on our snRNA-seq results, we adopted a protocol involving a single injection at 4 dpi. In DHM-treated mice, astrocytes were no longer confined to the edge of the fibrotic ECM but instead shifted their position into the fibrotic ECM, forming a smaller, more centrally located glial scar (Fig. 3a–d). Furthermore, neuronal tracing with adeno-associated virus (AAV)-*Cag-tdTomato* injection into the sensorimotor cortex at 14 dpi revealed that the glial scar volume reduction induced by DHM led to extensive axonal regeneration (Fig. 3e–f). The smaller glial scar volume was associated with axonal regeneration and consequently improved motor function (Fig. 3g-h, Supplementary Fig. 3). In order to analyze the direct effect of ADGRG1 inhibition on astrocytes, we designed an AAV expressing a short hairpin RNA targeting *Adgrg1* (*Adgrg1* K.D) (Supplementary Fig. 4) and injected it intraspinally 7 days prior to SCI. Similar to pharmacological inhibition, genetic knockdown of *Adgrg1* led to astrocytes entering the fibrotic ECM and forming a smaller, more compact scar (Fig. 3i–k). Notably, these structural changes were accompanied by improved motor function recovery compared to control AAV-treated animals (Fig. 3l). These results indicate that the type III collagen–astrocytic ADGRG1 axis controls the spatial organization of astrocytes after SCI, and that inhibiting this pathway promotes beneficial remodeling of the glial scar.

Astrocyte migration is impaired by the type III collagen–ADGRG1 axis

Given that ADGRG1 inhibition allowed astrocytes to enter the fibrotic ECM after SCI, we sought to elucidate the underlying mechanism using an *in vitro* model. Primary cultured astrocytes were first converted into a reactive phenotype and then plated under three different conditions: poly-L-lysine coating (control group), type III collagen coating (type III collagen group), and type III collagen coating with dihydromunduletone (DHM) treatment (DHM group) [16]. The migration ability of astrocytes was evaluated using a scratch assay. In the type III collagen group, we observed impaired astrocytic migration, while DHM treatment restored migration ability (Fig. 4a–b). To assess the movement of individual cells, we next performed a single-cell tracking assay. This analysis revealed shorter process lengths in the type III collagen group (Fig. 4c, Supplementary Fig. 5). Cells migrate through the following stages: the protrusion of processes at the leading edge of the cell, the adhesion of processes to the substrate, and cytoskeletal contraction [37]. Therefore, the shorter the processes, the less distance the cell can migrate in a single motion. Conversely, in the DHM group, astrocytes exhibited a mixture of short and long processes. There was no significant difference in the distance of cell migration and mean speed between the DHM group and the control group, respectively (Fig. 4d, Supplementary Fig. 6). Since the type III collagen-ADGRG1 pathway is known to regulate cell migration *via* RhoA-GTP binding, we next evaluated RhoA–GTP binding levels in each group. The type III collagen group showed elevated levels of RhoA–GTP binding relative to the control group, but no significant differences were observed in RhoA–GTP binding levels between the DHM group and the control group (Fig. 4e). Furthermore, to compare the effects of different collagen subtypes on astrocyte migration, we performed a cell migration assay. We

found that astrocytes cultured on type III collagen displayed significantly reduced migratory capacity compared to those on type I or type IV collagen (Fig. 4f–g). These findings indicate that type III collagen activates the ADGRG1–RhoA pathway to position astrocytes along the edge of the fibrotic ECM after SCI, and that pathway inhibition enables astrocytes to migrate into the fibrotic ECM, which leads to an inward shift of the glial scar position, resulting in a smaller glial scar.

Potential therapeutic efficacy of ADGRG1 antagonism in human SCI

Human induced pluripotent stem cells (hiPSCs) have been increasingly utilized in drug screening applications in recent years [38]. Using astrocytes derived from hiPSCs, we evaluated the potential of ADGRG1 blockade for human clinical application. These hiPSC-derived astrocytes expressed GFAP and ADGRG1 (Fig. 5a–b). We divided the hiPSC-derived astrocytes into three groups: hiPSC-derived astrocytes cultured on poly-L-lysine coating (control group), type III collagen coating (type III collagen group), and type III collagen coating with DHM treatment (DHM group). The migration ability of the hiPSC-derived astrocytes was assessed using scratch assays and single-cell tracking assays. Type III collagen suppressed the migration ability of hiPSC-derived astrocytes and importantly, DHM treatment successfully restored their migration ability (Fig. 5c–f). These findings indicate that the type III collagen-ADGRG1 pathway affects cell migration in human astrocytes, highlighting its potential therapeutic applications in human SCI.

Discussion

In this study, we used single-nucleus RNA sequencing, pathological analysis, and time-lapse imaging of astrocytes to address what stops migrating astrocytes at the edge of the fibrotic ECM and thereby builds the bilayered scar. We found that type III collagen suppressed astrocytic migration through the ADGRG1–RhoA pathway, thereby keeping reactive astrocytes at the edge of the fibrotic ECM. Inhibition of ADGRG1 allowed astrocytes to enter the fibrotic ECM, resulting in the formation of smaller glial scars in the fibrotic ECM and better motor function recovery. These results indicate that the type III collagen–ADGRG1 axis is a previously unrecognized signal that positions astrocytes during CNS scar formation. ADGRG1 has the potential to be a therapeutic target for SCI for several reasons.

First, the shift in glial scar formation toward the interior of the fibrotic ECM—achieved by blockade of the type III collagen–ADGRG1 pathway—may be beneficial, considering the recently recognized dual role of glial scars. While glial scars can serve as physical barriers to axon regeneration, glial scars also have a beneficial effect on axonal growth by sealing inflammatory cells within the glial scar [18]. Therefore, simply removing glial scars is not necessarily beneficial [39]. ADGRG1 inhibition may be advantageous in that it reduces the area enclosed by the glial scar while preserving the glial scar itself.

Second, ADGRG1 inhibition promoted axon regeneration by changing the distribution of reactive astrocytes. In the DHM injection group, compact glial scars formed more centrally within the fibrotic

ECM, creating spaces rather than glial scars at the lesion site. These spaces appeared to be filled by reactive astrocytes, which may have contributed to creating a more permissive environment for axonal growth. Consistent with this notion, corticospinal tract (CST) fibers in the DHM injection group frequently projected across the lesion site and, on the caudal side, often took alternative routes rather than passing through the dorsal column (Fig. 3e). Since CST axons in mice typically traverse the dorsal column [40], this observation suggests the formation of new detour circuits rather than mere sparing of pre-existing fibers, supporting true axonal regeneration.

Finally, our study identified type III collagen–ADGRG1 interaction as a critical upstream event that drives excessive activation of RhoA, thereby holding astrocytes at the edge of the fibrotic ECM. Because both excessive and insufficient RhoA activity can impair cell migration [41, 42], direct manipulation of RhoA may be suboptimal. Targeting the upstream cause of excessive activation—binding of type III collagen to ADGRG1—may therefore be a more effective and physiologically balanced strategy than conventional approaches aimed at RhoA itself.

ADGRG1 is known to bind different ligands and exert diverse functions in a cell type-specific manner. In astrocytes, type III collagen serves as a ligand, regulating migration inhibition and spatial positioning as demonstrated in this study. In contrast, in oligodendrocyte precursor cells (OPC), microglia-derived TG2 activates ADGRG1 in the presence of laminin, promoting OPC proliferation and differentiation into oligodendrocytes [13]. OPC-specific deletion of *Adgrg1* has been reported to reduce the number of myelinated axons [43], indicating that ADGRG1 plays an important role in remyelination through OPCs. After SCI, remyelination begins in earnest after 2 weeks post-injury, with oligodendrogenesis peaking at 4–7 weeks and new myelin formation reaching its maximum at 3 months [44, 45]. In this study, a single DHM administration at 4 dpi yielded favorable results, including spatial redistribution of astrocytes and enhanced axonal regeneration. Our snRNA-seq data revealed that ADGRG1 is highly expressed in astrocytes, whereas its expression in OPCs is comparatively low (Supplementary Fig. 2), suggesting that astrocytes represent the primary cellular target of DHM. Furthermore, this administration timing precedes the onset of active remyelination, suggesting that the impact on OPCs may have been limited. Nevertheless, prolonged ADGRG1 inhibition during the chronic phase cannot entirely exclude the possibility of impairing OPC-mediated remyelination. Developing astrocyte-specific ADGRG1 inhibition strategies and optimizing administration timing and duration will be important challenges for future therapeutic applications.

Spatial transcriptomic analysis in this study revealed that *Col3a1* is predominantly expressed in VLMC and ABC clusters in close proximity to astrocytes. These cells are fibroblast-like cells derived from the meninges and perivascular spaces and have been reported to invade the lesion core after SCI and become major components of the fibrotic scar [6, 46]. Recent scRNA-seq and lineage-tracing studies have demonstrated that these fibroblasts represent a heterogeneous population, with meningeal-derived fibroblasts predominantly localized in the central region of the scar and perivascular fibroblasts localized at the periphery [47]. Consistent with this spatial segregation, our data suggest that VLMC_1, which are likely of perivascular origin, were distributed broadly throughout the spinal cord, whereas ABC_1 and 2,

presumed to be of arachnoid origin, were concentrated in the lesion core. Furthermore, *Col3a1* expression was markedly higher in ABCs than in VLMC, and at 7 days post-injury, ABC_2 exhibited the highest ADGRG1-mediated interaction scores among all fibroblast subclusters. Taken together, these findings raise the possibility that the spatial restriction of astrocytes to the lesion periphery — where they form the surrounding glial scar rather than infiltrating the lesion center — is partly determined by the cellular source of type III collagen secretion. The spatial gradient of *Col3a1* expression, from the peripherally distributed VLMCs to the centrally concentrated ABCs, may thus represent a key determinant of the spatial boundary between the fibrotic and glial scar compartments.

Our study has several limitations. First, we examined only a single injury type: the contusion model. In the contusion model, the lesion is extensive, and astrocyte migration is required to fill the defect area. Therefore, the blockade of the type III collagen-ADGRG1 pathway was likely beneficial in this study. By contrast, in a narrow stab injury, where the tissue defect is small and little migration occurs, ADGRG1 blockade may not yield particularly favorable results. Indeed, the astrocyte behavior after injury appears to depend on the injury type: Okada *et al*. reported that reactive astrocytes migrate to form the glial scar after widespread contusion of the spinal cord[18], whereas Bardehle *et al.* reported that, after a narrow stab injury made with a thin knife, astrocytes did not migrate towards the lesion but instead proliferated at juxtavascular sites[48]. Hence, in other types of injury, the benefit of ADGRG1 blockade may be limited.

Second, astrocyte-specific *Adgrg1* knockdown was achieved using an AAV driven by the *Gfap* promoter. Although this is the most widely used tool for targeting astrocytes, it does not resolve the heterogeneity of astrocytes in the injured spinal cord. Future genetic interventions targeting specific astrocyte subclusters -such as Astro_6, the reactive population that becomes dominant during the acute phase - would provide more precise insight.

Finally, our hiPSC-derived astrocyte experiments demonstrate the translational relevance of the type III collagen–ADGRG1 pathway, but the hiPSC line used in this study derives from a single genetic background. Because genetic variation may influence ADGRG1 expression levels and pathway activity, an important next step toward clinical translation will be to validate our findings in multiple independent hiPSC lines derived from donors with diverse genetic backgrounds, including different ethnic populations.

In conclusion, type III collagen holds reactive astrocytes at the edge of the fibrotic ECM *via* the astrocytic ADGRG1–RhoA pathway, thereby organizing the bilayered architecture of the CNS scar. ADGRG1 blockade shifts the positioning of glial scar formation from the edge of the fibrotic ECM into its interior, reducing glial scar volume and facilitating axonal regeneration. These findings identify the type III collagen–ADGRG1 axis as a previously unrecognized organizer of glial scar architecture and as a potential therapeutic target for modulating maladaptive scarring after traumatic CNS injury.

Declarations

Ethics approval and consent to participate

All animal experiments were approved by the Institutional Animal Care and Use Committee of Kyushu University Graduate School of Medical Sciences (Approval No. A22-274-2) and were performed in accordance with the institution's Regulation for Animal Experiments, the Principles of Laboratory Animal Care, and the relevant Japanese national laws (the Act on Welfare and Management of Animals). The study complies with the ARRIVE guidelines 2.0.

Consent for publication

Not applicable

Availability of data and materials

Raw experimental data generated in this study are provided in the source data accompanying this paper. For the RNA sequencing analyses, publicly available data from the Gene Expression Omnibus (GEO) under accession number GSE234774 were utilized. All data necessary to reproduce the findings of this study are included in the source data. All analysis code used in this study is publicly available at https://github.com/onogentaro/ADGRG1-blockade-drives-astrocytes-into-the-extracellular-matrix-to-reduce-glial-scar-size and permanently archived at Zenodo (https://doi.org/10.5281/zenodo.20395684). Any additional information required for reanalysis is available from the corresponding author upon reasonable request.

Competing interests

The authors report no competing interests.

Funding

This study was supported by Japan Society for the Promotion of Science (JSPS) KAKENHI under Grant Numbers JP18K16665, JP19K18515, JP22K09426, JP22K19587, JP23K27722, and JP23H03031; the Japan Science and Technology Agency (JST) FOREST Program under Grant Number JPMJFR220P; ZENKYOREN (National Mutual Insurance Federation of Agricultural Cooperatives); the Takeda Science Foundation; and the General Insurance Association of Japan.

Author contributions

Gentaro Ono performed the experiments, analyzed the data, and wrote the original draft. Kazu Kobayakawa, Hirokazu Saiwai, and Kazuya Yokota supervised the research design and reviewed the manuscript. Tetsuya Tamaru, Kazuhiro Hata, Hirotaka Iura, Yohei Haruta, Kazuki Kitade, and Jun Kishikawa assisted with *in vivo* experiments and tissue analysis. Kiyoshi Tarukado, Kenichi Kawaguchi, Takeshi Maeda, Seiji Okada, and Yasuharu Nakashima provided clinical and conceptual input. Dai-Jiro Konno and Kinichi Nakashima provided guidance on the experimental technology. Kazu Kobayakawa designed the studies, supervised the overall project, and prepared the final version of the manuscript. All authors have read and approved the final manuscript.

Acknowledgments

We thank Y. Gotoh for providing the Aldh1l1-EGFP mice. We also appreciate the technical assistance from the Research Support Center and the Research Center for Human Disease Modeling at Kyushu University Graduate School of Medical Sciences.

References

1. Burda JE, Sofroniew M V. Reactive Gliosis and the Multicellular Response to CNS Damage and Disease. Neuron. Cell Press; 2014;81:229–48. https://doi.org/10.1016/j.neuron.2013.12.034
2. Wanner IB, Anderson MA, Song B, Levine J, Fernandez A, Gray-Thompson Z, et al. Glial Scar Borders Are Formed by Newly Proliferated, Elongated Astrocytes That Interact to Corral Inflammatory and Fibrotic Cells via STAT3-Dependent Mechanisms after Spinal Cord Injury. J Neurosci [Internet]. Society for Neuroscience; 2013 [cited 2023 Jun 29];33:12870–86. https://doi.org/10.1523/jneurosci.2121-13.2013
3. Silver J, Miller JH. Regeneration beyond the glial scar. Nat Rev Neurosci [Internet]. Nat Rev Neurosci; 2004 [cited 2022 Apr 26];5:146–56. https://doi.org/10.1038/nrn1326
4. Sofroniew M V. Astrocyte Reactivity: Subtypes, States, and Functions in CNS Innate Immunity. Trends Immunol [Internet]. Elsevier; 2020 [cited 2024 Jan 9];41:758–70. https://doi.org/10.1016/j.it.2020.07.004
5. Hara M, Kobayakawa K, Ohkawa Y, Kumamaru H, Yokota K, Saito T, et al. Interaction of reactive astrocytes with type I collagen induces astrocytic scar formation through the integrin–N-cadherin pathway after spinal cord injury. Nat Med [Internet]. Nature Publishing Group; 2017 [cited 2022 May 23];23:818–28. https://doi.org/10.1038/nm.4354
6. Soderblom C, Luo X, Blumenthal E, Bray E, Lyapichev K, Ramos J, et al. Perivascular Fibroblasts Form the Fibrotic Scar after Contusive Spinal Cord Injury. J Neurosci [Internet]. 2013 [cited 2026 Feb 15];33:13882–7. https://doi.org/10.1523/jneurosci.2524-13.2013
7. Hamann J, Aust G, Araç D, Engel FB, Formstone C, Fredriksson R, et al. International Union of Basic and Clinical Pharmacology. XCIV. Adhesion G Protein–Coupled Receptors. Pharmacol Rev [Internet]. American Society for Pharmacology and Experimental Therapy; 2015 [cited 2026 Feb 13];67:338–67. https://doi.org/10.1124/pr.114.009647
8. Langenhan T, Aust G, Hamann J. Sticky signaling--adhesion class G protein-coupled receptors take the stage. Sci Signal [Internet]. Sci Signal; 2013 [cited 2026 Feb 13];6. https://doi.org/10.1126/scisignal.2003825
9. Salzman GS, Ackerman SD, Ding C, Koide A, Leon K, Luo R, et al. Structural basis for regulation of GPR56/ADGRG1 by its alternatively spliced extracellular domains. Neuron [Internet]. Cell Press; 2016 [cited 2026 Feb 13];91:1292–304. https://doi.org/10.1016/j.neuron.2016.08.022
10. Luo R, Jeong SJ, Jin Z, Strokes N, Li S, Piao X. G protein-coupled receptor 56 and collagen III, a receptor-ligand pair, regulates cortical development and lamination. Proc Natl Acad Sci U S A

[Internet]. Proc Natl Acad Sci U S A; 2011 [cited 2026 Feb 13];108:12925–30. https://doi.org/10.1073/pnas.1104821108

11. Luo R, Jeong SJ, Yang A, Wen M, Saslowsky DE, Lencer WI, et al. Mechanism for adhesion G protein-coupled receptor GPR56-mediated RhoA activation induced by collagen III stimulation. PLoS One [Internet]. PLoS One; 2014 [cited 2026 Feb 13];9. https://doi.org/10.1371/journal.pone.0100043
12. Li T, Chiou B, Gilman CK, Luo R, Koshi T, Yu D, et al. A splicing isoform of GPR56 mediates microglial synaptic refinement via phosphatidylserine binding. EMBO J [Internet]. EMBO J; 2020 [cited 2026 Feb 13];39. https://doi.org/10.15252/embj.2019104136
13. Giera S, Deng Y, Luo R, Ackerman SD, Mogha A, Monk KR, et al. The adhesion G protein-coupled receptor GPR56 is a cell-autonomous regulator of oligodendrocyte development. Nat Commun [Internet]. Nat Commun; 2015 [cited 2026 Feb 13];6. https://doi.org/10.1038/ncomms7121
14. Giera S, Luo R, Ying Y, Ackerman SD, Jeong SJ, Stoveken HM, et al. Microglial transglutaminase-2 drives myelination and myelin repair via GPR56/ADGRG1 in oligodendrocyte precursor cells. Elife [Internet]. eLife Sciences Publications Ltd; 2018 [cited 2026 Feb 13];7:e33385. https://doi.org/10.7554/elife.33385
15. Kobayakawa K, Kumamaru H, Saiwai H, Kubota K, Ohkawa Y, Kishimoto J, et al. Acute hyperglycemia impairs functional improvement after spinal cord injury in mice and humans. Sci Transl Med [Internet]. Sci Transl Med; 2014 [cited 2022 May 10];6. https://doi.org/10.1126/scitranslmed.3009430
16. Stoveken HM, Bahr LL, Anders MW, Wojtovich AP, Smrcka A V., Tall GG. Dihydromunduletone is a small-molecule selective adhesion G protein-coupled receptor antagonists. Mol Pharmacol [Internet]. American Society for Pharmacology and Experimental Therapy; 2016 [cited 2025 Jul 1];90:214–24. https://doi.org/10.1124/mol.116.104828
17. Schildge S, Bohrer C, Beck K, Schachtrup C. Isolation and Culture of Mouse Cortical Astrocytes. J Vis Exp [Internet]. 2013 [cited 2022 Jun 13];e50079. https://doi.org/10.3791/50079
18. Okada S, Nakamura M, Katoh H, Miyao T, Shimazaki T, Ishii K, et al. Conditional ablation of Stat3 or Socs3 discloses a dual role for reactive astrocytes after spinal cord injury. Nat Med [Internet]. Nature Publishing Group; 2006 [cited 2022 Apr 26];12:829–34. https://doi.org/10.1038/nm1425
19. Kijima K, Kubota K, Hara M, Kobayakawa K, Yokota K, Saito T, et al. The acute phase serum zinc concentration is a reliable biomarker for predicting the functional outcome after spinal cord injury. EBioMedicine. Elsevier B.V.; 2019;41:659–69. https://doi.org/10.1016/j.ebiom.2019.03.003
20. Kijima K, Ono G, Kobayakawa K, Saiwai H, Hara M, Yoshizaki S, et al. Zinc deficiency impairs axonal regeneration and functional recovery after spinal cord injury by modulating macrophage polarization via NF-κB pathway. Front Immunol [Internet]. Frontiers Media SA; 2023 [cited 2026 Mar 18];14:1290100. https://doi.org/10.3389/fimmu.2023.1290100
21. Hirota R, Sasaki M, Kataoka-Sasaki Y, Oshigiri T, Kurihara K, Fukushi R, et al. Enhanced Network in Corticospinal Tracts after Infused Mesenchymal Stem Cells in Spinal Cord Injury. J Neurotrauma

[Internet]. Mary Ann Liebert Inc; 2022 [cited 2023 Jan 6];39:1665–81. https://doi.org/10.1089/neu.2022.0106

22. Saiwai H, Ohkawa Y, Yamada H, Kumamaru H, Harada A, Okano H, et al. The LTB4-BLT1 axis mediates neutrophil infiltration and secondary injury in experimental spinal cord injury. Am J Pathol. 2010;176:2352–66. https://doi.org/10.2353/ajpath.2010.090839
23. Skinnider MA, Gautier M, Teo AYY, Kathe C, Hutson TH, Laskaratos A, et al. Single-cell and spatial atlases of spinal cord injury in the Tabulae Paralytica. Nature [Internet]. Nature; 2024 [cited 2025 Apr 28];631:150–63. https://doi.org/10.1038/s41586-024-07504-y
24. Wolf FA, Angerer P, Theis FJ. SCANPY: Large-scale single-cell gene expression data analysis. Genome Biol [Internet]. BioMed Central Ltd.; 2018 [cited 2023 Nov 18];19:1–5. https://doi.org/10.1186/s13059-017-1382-0
25. Domínguez Conde C, Xu C, Jarvis LB, Rainbow DB, Wells SB, Gomes T, et al. Cross-tissue immune cell analysis reveals tissue-specific features in humans. Science (1979) [Internet]. American Association for the Advancement of Science; 2022 [cited 2025 Apr 29];376. https://doi.org/10.1126/science.abl5197
26. Xu C, Prete M, Webb S, Jardine L, Stewart BJ, Hoo R, et al. Automatic cell-type harmonization and integration across Human Cell Atlas datasets. Cell [Internet]. Elsevier B.V.; 2023 [cited 2025 Apr 29];186:5876-5891.e20. https://doi.org/10.1016/j.cell.2023.11.026
27. Yao Z, van Velthoven CTJ, Kunst M, Zhang M, McMillen D, Lee C, et al. A high-resolution transcriptomic and spatial atlas of cell types in the whole mouse brain. Nature [Internet]. Nature Publishing Group; 2023 [cited 2025 Apr 29];624:317–32. https://doi.org/10.1038/s41586-023-06812-z
28. Garcia-Alonso L, Lorenzi V, Mazzeo CI, Alves-Lopes JP, Roberts K, Sancho-Serra C, et al. Single-cell roadmap of human gonadal development. Nature [Internet]. Nature Publishing Group; 2022 [cited 2023 Nov 14];607:540–7. https://doi.org/10.1038/s41586-022-04918-4
29. Olsen ML, Campbell SC, McFerrin MB, Floyd CL, Sontheimer H. Spinal cord injury causes a wide-spread, persistent loss of Kir4.1 and glutamate transporter 1: benefit of 17 beta-oestradiol treatment. Brain [Internet]. Brain; 2010 [cited 2026 Mar 3];133:1013–25. https://doi.org/10.1093/brain/awq049
30. Nagelhus EA, Ottersen OP. Physiological Roles of Aquaporin-4 in Brain. Physiol Rev [Internet]. 2013 [cited 2026 Mar 3];93:1543–62. https://doi.org/10.1152/physrev.00011.2013
31. Zamanian JL, Xu L, Foo LC, Nouri N, Zhou L, Giffard RG, et al. Genomic Analysis of Reactive Astrogliosis. The Journal of Neuroscience [Internet]. 2012 [cited 2026 Mar 3];32:6391–410. https://doi.org/10.1523/jneurosci.6221-11.2012
32. Zhao Q, Ren YL, Zhu YJ, Huang RQ, Zhu RR, Cheng LM, et al. The origins and dynamic changes of C3- and S100A10-positive reactive astrocytes after spinal cord injury. Front Cell Neurosci [Internet]. Frontiers Media SA; 2023 [cited 2026 Mar 3];17:1276506. https://doi.org/10.3389/fncel.2023.1276506

33. Liddelow SA, Guttenplan KA, Clarke LE, Bennett FC, Bohlen CJ, Schirmer L, et al. Neurotoxic reactive astrocytes are induced by activated microglia. Nature [Internet]. Nature Publishing Group; 2017 [cited 2026 Feb 14];541:481–7. https://doi.org/10.1038/nature21029
34. Rios C, Santander I, Méndez-Armenta M, Nava-Ruiz C, Orozco-Suárez S, Islas M, et al. Metallothionein-I + II Reduces Oxidative Damage and Apoptosis after Traumatic Spinal Cord Injury in Rats. Oxid Med Cell Longev [Internet]. Hindawi Limited; 2018 [cited 2026 Mar 3];2018:3265918. https://doi.org/10.1155/2018/3265918
35. O'Shea TM, Ao Y, Wang S, Ren Y, Cheng AL, Kawaguchi R, et al. Derivation and transcriptional reprogramming of border-forming wound repair astrocytes after spinal cord injury or stroke in mice. Nat Neurosci [Internet]. Nature Research; 2024 [cited 2026 Mar 3];27:1505–21. https://doi.org/10.1038/s41593-024-01684-6
36. Habib N, McCabe C, Medina S, Varshavsky M, Kitsberg D, Dvir-Szternfeld R, et al. Disease-associated astrocytes in Alzheimer's disease and aging. Nat Neurosci [Internet]. Nature Research; 2020 [cited 2026 Mar 26];23:701–6. https://doi.org/10.1038/s41593-020-0624-8
37. SenGupta S, Parent CA, Bear JE. The principles of directed cell migration. Nat Rev Mol Cell Biol [Internet]. NIH Public Access; 2021 [cited 2023 Jul 28];22:529–47. https://doi.org/10.1038/s41580-021-00366-6
38. Silva MC, Haggarty SJ. Human pluripotent stem cell–derived models and drug screening in CNS precision medicine. Ann N Y Acad Sci [Internet]. John Wiley & Sons, Ltd; 2020 [cited 2024 Jan 19];1471:18–56. https://doi.org/10.1111/nyas.14012
39. Anderson MA, Burda JE, Ren Y, Ao Y, O'Shea TM, Kawaguchi R, et al. Astrocyte scar formation aids CNS axon regeneration. Nature [Internet]. NIH Public Access; 2016 [cited 2022 Apr 24];532:195–200. https://doi.org/10.1038/nature17623
40. Moreno-Lopez Y, Bichara C, Delbecq G, Isope P, Cordero-Erausquin M. The corticospinal tract primarily modulates sensory inputs in the mouse lumbar cord. Elife [Internet]. eLife Sciences Publications Ltd; 2021 [cited 2025 Jun 20];10:e65304. https://doi.org/10.7554/elife.65304
41. Renault-Mihara F, Okano H. STAT3-regulated RhoA drives reactive astrocyte dynamics. Cell Cycle. Taylor and Francis Inc.; 2017;16:1995–6. https://doi.org/10.1080/15384101.2017.1377032
42. Ray RM, Patel A, Viar MJ, McCormack SA, Zheng Y, Tigyi G, et al. RhoA inactivation inhibits cell migration but does not mediate the effects of polyamine depletion. Gastroenterology. W.B. Saunders; 2002;123:196–205. https://doi.org/10.1053/gast.2002.34216
43. Chiou B, Gao C, Giera S, Folts CJ, Kishore P, Yu D, et al. Cell type-specific evaluation of ADGRG1/GPR56 function in developmental central nervous system myelination. Glia [Internet]. Glia; 2021 [cited 2026 Feb 15];69:413–23. https://doi.org/10.1002/glia.23906
44. Duncan GJ, Manesh SB, Hilton BJ, Assinck P, Liu J, Moulson A, et al. Locomotor recovery following contusive spinal cord injury does not require oligodendrocyte remyelination. Nat Commun [Internet]. Nature Publishing Group; 2018 [cited 2026 Feb 15];9:3066. https://doi.org/10.1038/s41467-018-05473-1

45. Hesp ZC, Goldstein EA, Miranda CJ, Kaspar BK, McTigue DM. Chronic Oligodendrogenesis and Remyelination after Spinal Cord Injury in Mice and Rats. J Neurosci [Internet]. Society for Neuroscience; 2015 [cited 2026 Feb 15];35:1274–90. https://doi.org/10.1523/jneurosci.2568-14.2015
46. Dorrier CE, Jones HE, Pintarić L, Siegenthaler JA, Daneman R. Emerging roles for CNS fibroblasts in health, injury and disease. Nat Rev Neurosci [Internet]. Nature Research; 2022 [cited 2026 Feb 15];23:23–34. https://doi.org/10.1038/s41583-021-00525-w
47. Xue X, Wu X, Fan Y, Han S, Zhang H, Sun Y, et al. Heterogeneous fibroblasts contribute to fibrotic scar formation after spinal cord injury in mice and monkeys. Nat Commun [Internet]. Nature Research; 2024 [cited 2026 Feb 15];15:6321. https://doi.org/10.1038/s41467-024-50564-x
48. Bardehle S, Krüger M, Buggenthin F, Schwausch J, Ninkovic J, Clevers H, et al. Live imaging of astrocyte responses to acute injury reveals selective juxtavascular proliferation. Nat Neurosci [Internet]. Nat Neurosci; 2013 [cited 2023 Mar 20];16:580–6. https://doi.org/10.1038/NN.3371

Figures

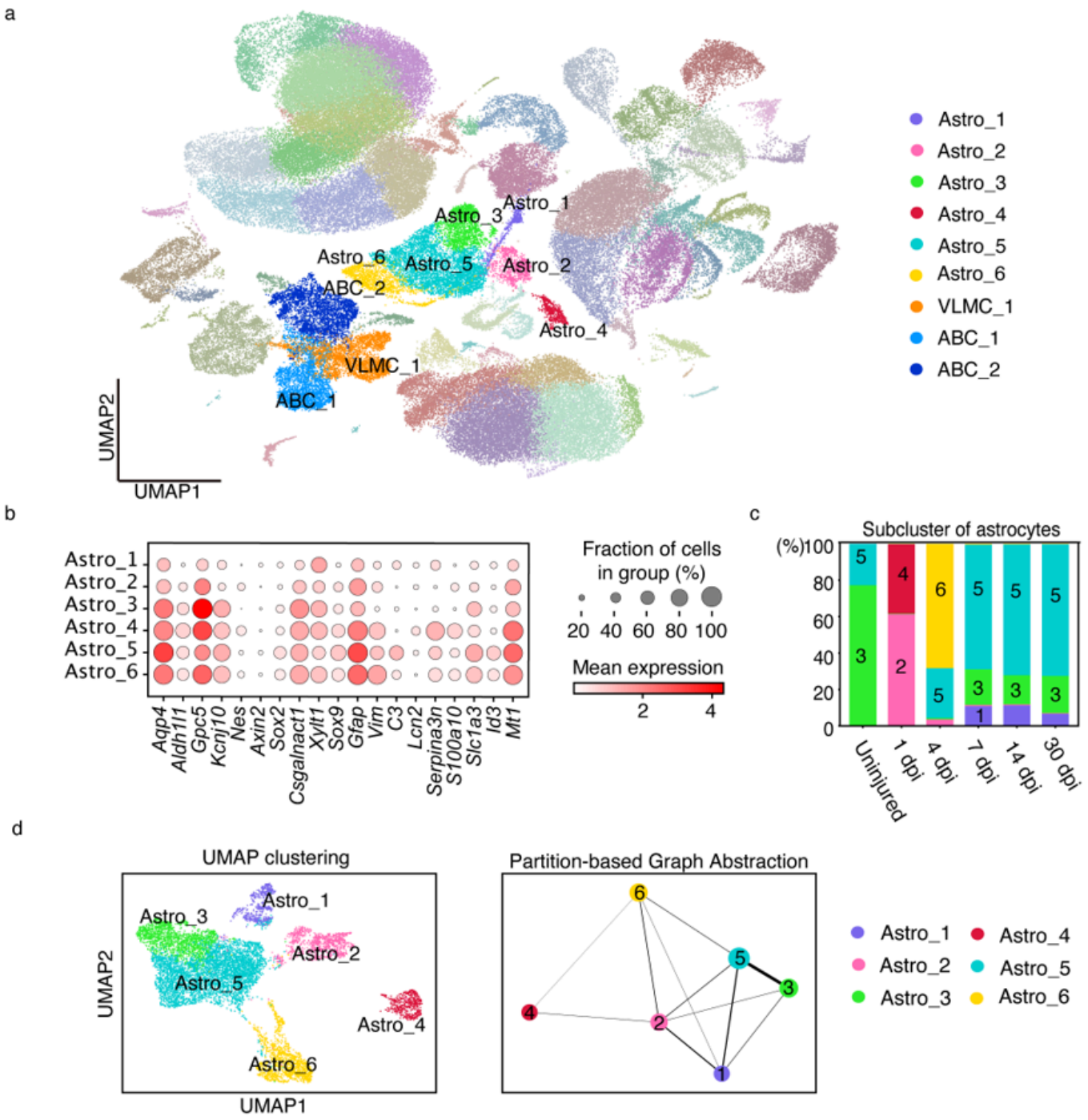


Figure 1

snRNA-seq analysis of astrocyte subclusters in the injured spinal cord

(a) UMAP of cell states (cell types) in the spinal cord snRNA-seq (*n* = 94292) datasets. Astro: Astrocytes, ABC: Arachnoid barrier cells, VLMC: vascular leptomeningeal cells. (b) Dot plots showing the snRNA-seq analysis results concerning gene expression in the subcluster of astrocytes. Color indicates the normalized mean gene expression; size reflects the fraction of cells in the subcluster. (c) Stacked bar

plot showing the temporal changes in the relative proportions of astrocyte subclusters. dpi: days post-injury. (d) UMAP of astrocyte state and Partition-based graph abstraction (PAGA) analysis of astrocyte subclusters in injured spinal cord, showing the connectivity and transition relationships between subpopulations. Subclusters are color-coded as follows: Astro_1 (purple), Astro_2 (pink), Astro_3 (green), Astro_4 (red), Astro_5 (cyan), and Astro_6 (yellow). Edge width is proportional to the connectivity score between clusters, with edges below a connectivity threshold of 0.01 omitted from visualization.

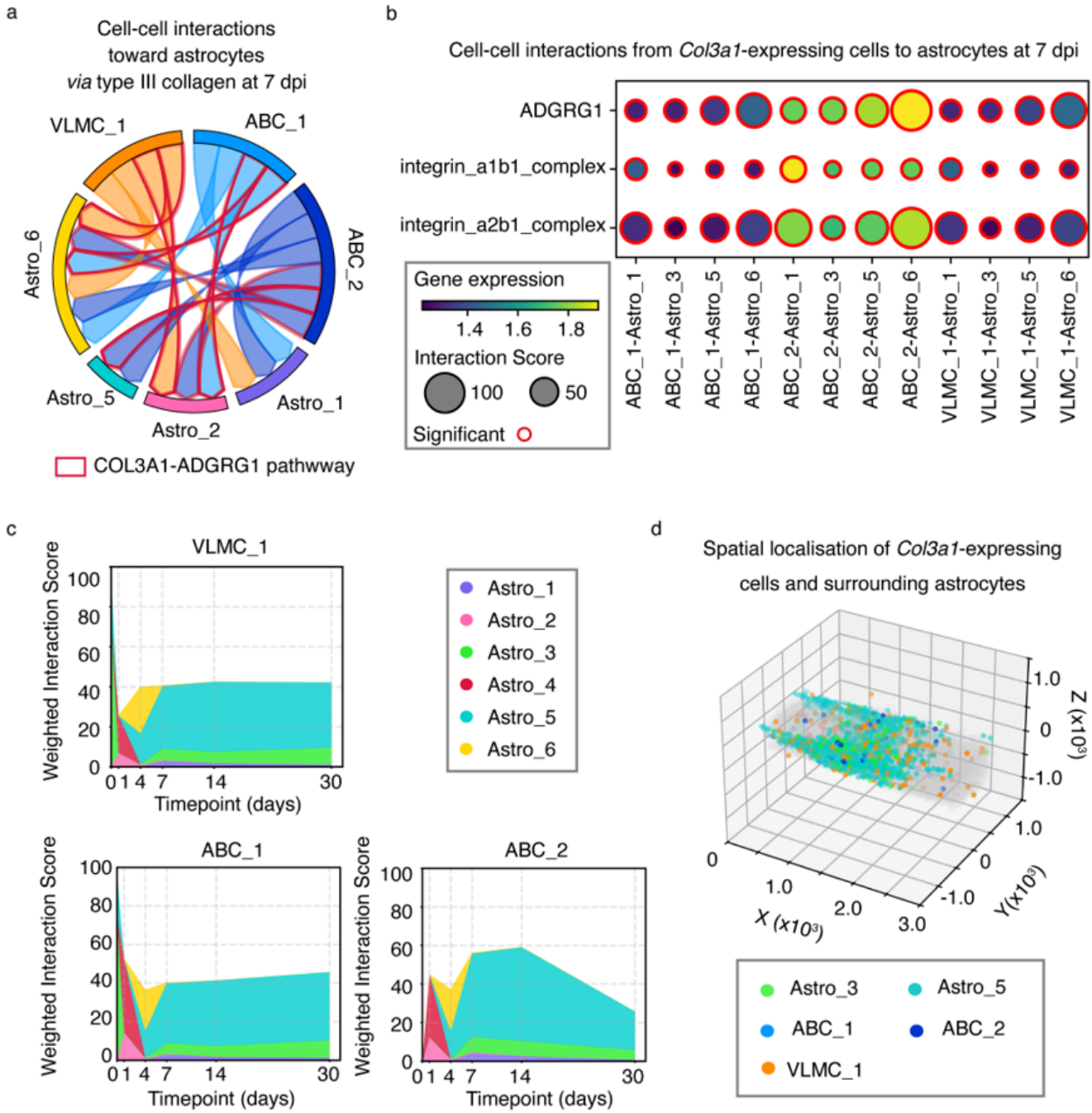


Figure 2

Cell-cell interaction between astrocytes and type III collagen–secreting cells

(a) Circos plots showing the number of significant and strong cell interactions *via* collagen in the injured spinal cord at 7 dpi. Numbers above the arrows indicate the number of pathways that were strong for each cell–cell pair. Arrows outlined in red indicate the type III collagen-ADGRG1 pathway. Interaction scores > 50 were considered strong. (b) Dot plots showing the snRNA-seq analysis results concerning cell-cell interactions at 7 dpi. Color indicates co-expression of ligand and astrocyte receptor genes; size reflects the interaction score; presence of a red outline indicates statistical significance. $P < 0.05$ were considered significant. (c) Stacked area chart showing the weighted interaction scores for each astrocyte subcluster across time points post-injury. Values were calculated by multiplying the interaction score by the relative proportion of each astrocyte subcluster at each time point. (d) 3D-spatial transcriptomics of the injured spinal cord at 7 dpi, highlighting type III collagen–secreting cells and neighboring astrocytes.

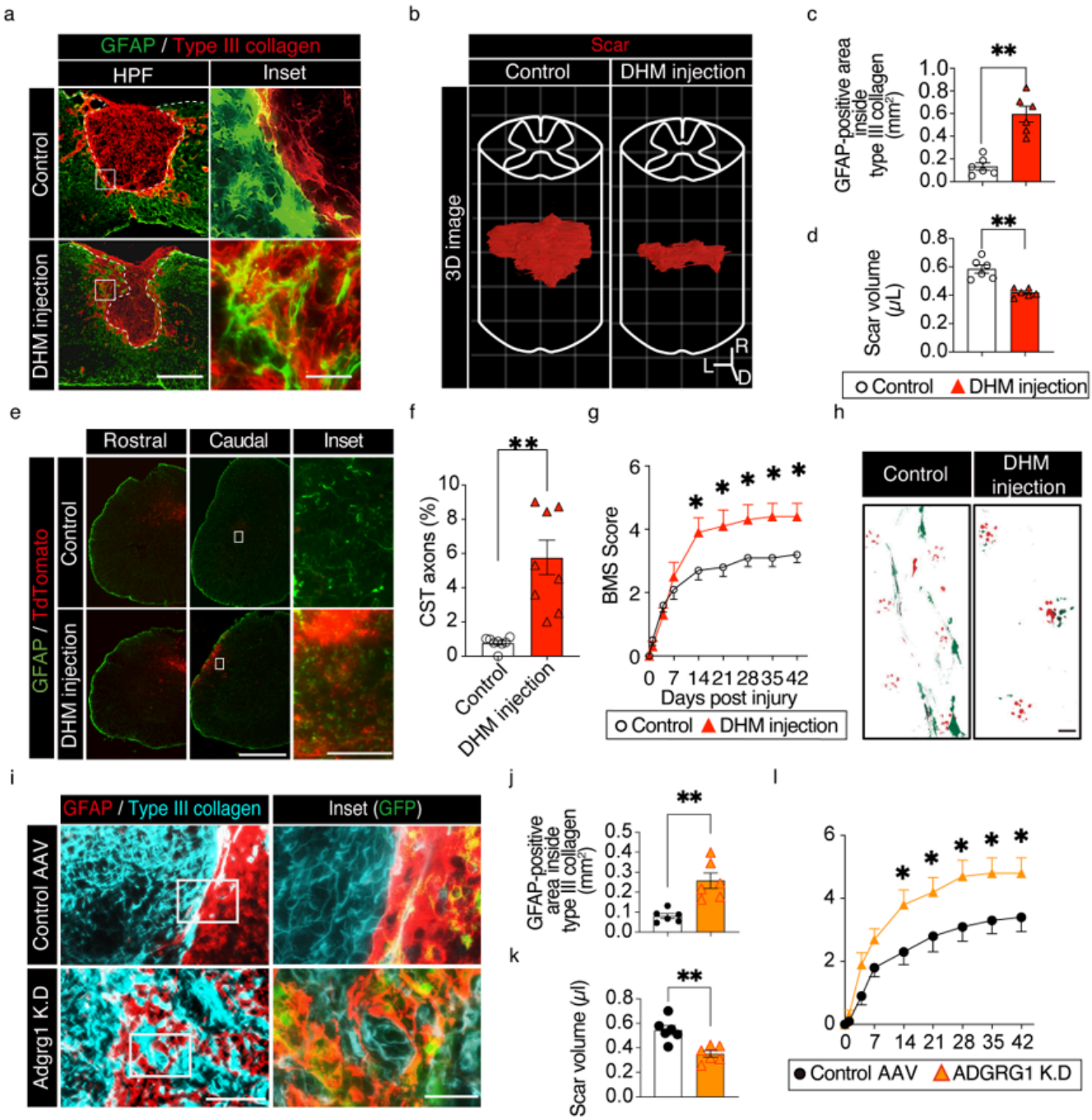


Figure 3

ADGRG1 inhibition reduces glial scar volume and improves motor outcome after SCI

(a) Representative images showing GFAP (green) and type III collagen (red) staining of spinal cords at 14 dpi receiving PBS (control group) or DHM (DHM injection group). The white dotted line indicates the border of the glial scar. Scale bars: 500 μm and 50 μm (inset). (b) Three-dimensional images of the scar in the control group and in the DHM injection group (red: type III collagen-positive volume surrounded by GFAP-positive area). R indicates the rostral side, D indicates the dorsal side, and L indicates the left side.

Grid size: 500 μm. (c) Quantitative analysis of the area of astrocytes inside type III collagen in the control group and in the DHM injection group (*n* = 6). (d) Quantitative analysis of scar volume between the control group and DHM injection group (*n* = 6). (e) Neuronal tracing images showing tdTomato (red)-positive axons and GFAP (green)-positive astrocytes in the control group and in the DHM inj group. Scale bars: 500 μm and 50 μm (inset). (f) Quantitative analysis of axons in the control group and in the DHM injection group (*n* = 8). (g) The time course of the BMS score after SCI in the control group and in the DHM injection group (*n* = 10). (h) Representative footprint images showing forelimb (red) and hindlimb (green) prints in the control and DHM injection groups. Scale bar: 5 mm. (i) Representative images showing GFAP (red), type III collagen (cyan), and GFP (green, inset) staining of spinal cords at 14 dpi, treated with control AAV (control AAV group) or AAV-*Gfap-shAdgrg1* (*Adgrg1* K.D group). Scale bars: 200 μm and 50 μm (inset). (j) Quantitative analysis of the area of astrocytes inside type III collagen in the control AAV group and in the *Adgrg1* K.D group (*n* = 6). (k) Quantitative analysis of scar volume between the control AAV group and the *Adgrg1* K.D group (*n*= 6). (l) The time course of the BMS score after SCI in the control AAV group and in the *Adgrg1* K.D group (*n*= 10). **P* < 0.05, ***P* < 0.005, unpaired t-test (c, d, f, j, and k), two-way ANOVA (g and l). Data represent the mean ± SEM (c, d, f, g, j, k, and l).

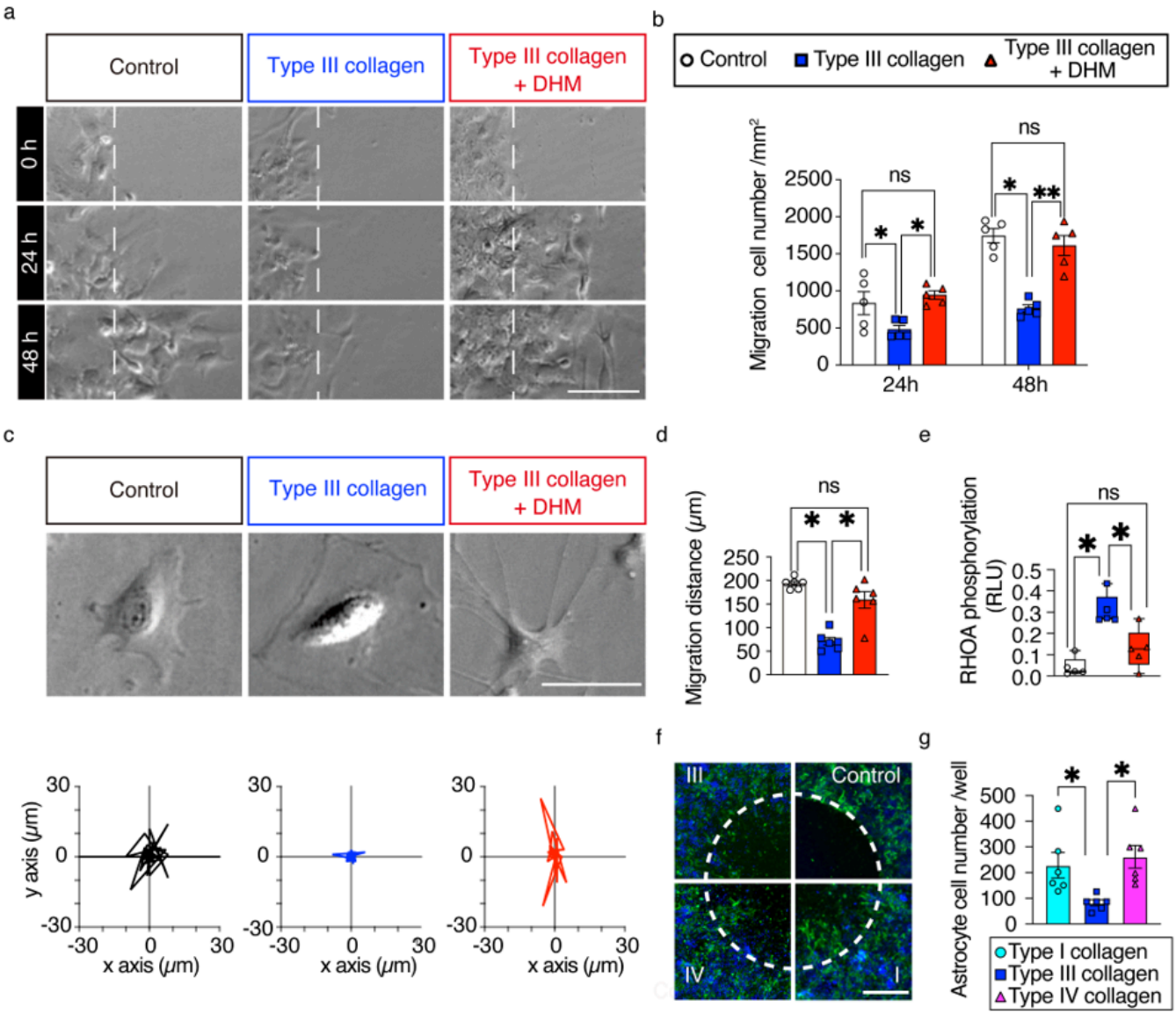


Figure 4

ADGRG1-type III collagen pathway controls astrocytic migration

(a) *In vitro* scratch injury of monolayer-cultured astrocytes on poly-L-lysine coating, type III collagen coating, or type III collagen coating with DHM. Scale bar: 100 μm. (b) Quantitative analysis of the number of migrating cells among the three groups (*n*= 10). (c) Representative images and migration plots of astrocytes from the single-cell tracking assay among the three groups. Scale bar: 50 μm. (d) Quantitative analysis of migration distance among the three groups in the single-cell tracking assay (*n* = 5). (e) Quantitative analysis of RhoA-GTP binding levels among the three groups (*n* = 5). (f) *In vitro* cell migration assay of monolayer-cultured astrocytes on type III, type I, or type IV collagen coating. Stopper intact: astrocytes cultured on type III collagen with the stopper kept until fixation. Representative images depicting GFAP (green) and Hoechst (blue). Scale bar: 500 μm. (g) Quantitative analysis of the number of

migrating cells among the three groups (n = 6). *P < 0.05, **P < 0.005, one-way ANOVA (b, d, e, g). Data represent the mean ± SEM (b, d, g). Data represent minimum to maximum (e).

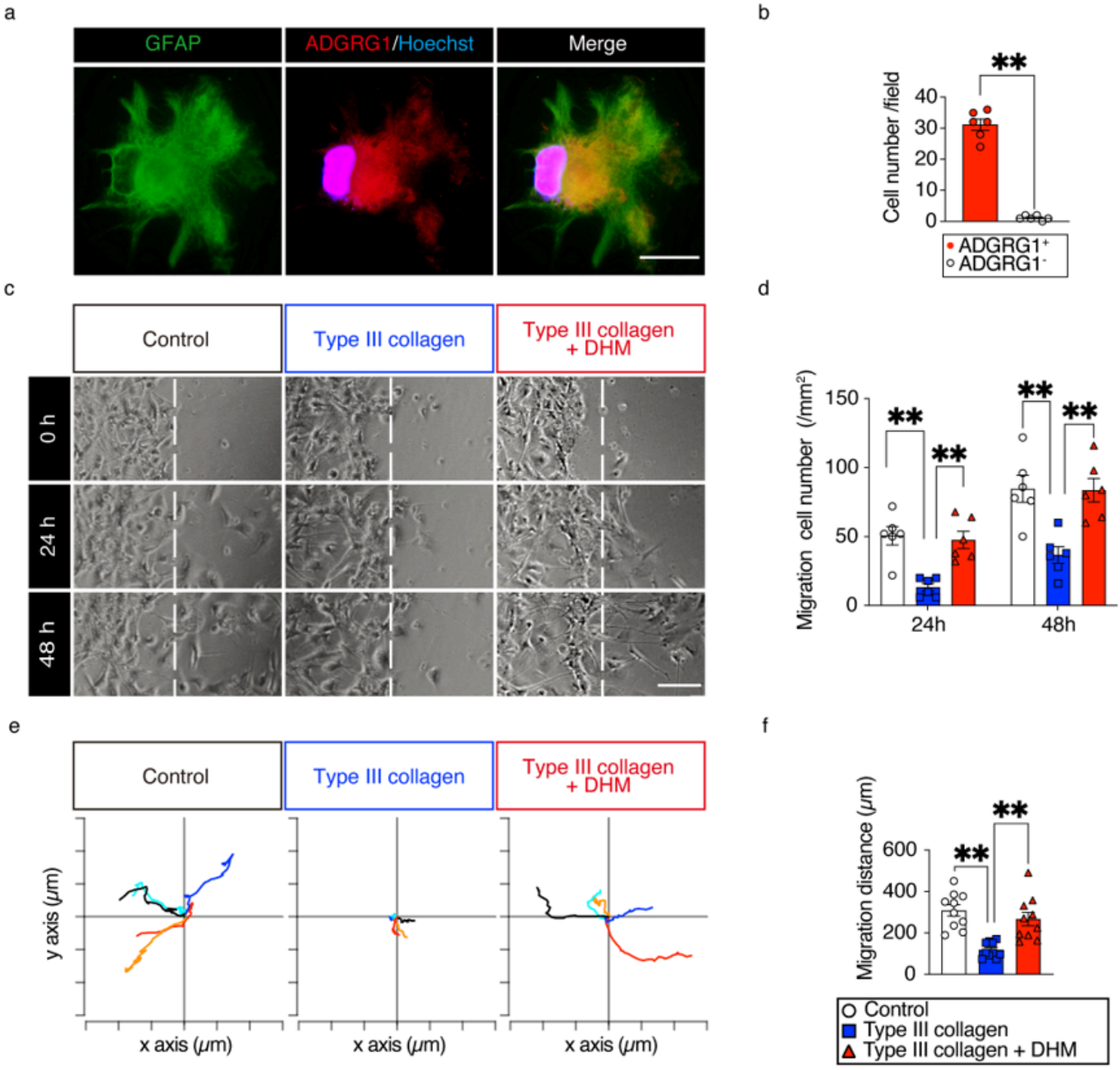


Figure 5

ADGRG1 blockade is effective against hiPSC-derived astrocytes.

(a) Representative images of hiPSC-derived astrocytes showing GFAP (green), ADGRG1 (red), and Hoechst (blue) staining. Scale bar: 20 μm. (b) Quantitative analysis of ADGRG1-positive hiPSC-derived astrocytes. (c) *In vitro* scratch assay with monolayer-cultured hiPSC-derived astrocytes on Geltrex

coating, type III collagen coating, or type III collagen coating with DHM. Scale bar: 500 μm. (d) Quantitative analysis of the number of migrating cells among the three groups in the scratch assay (n = 6). (e) Migration plots from the single-cell tracking assay of hiPSC-derived astrocytes (n= 5). The tick interval is 100 μm. (f) Quantitative analysis of the migration distance among the three groups (n = 10). *P < 0.05, **P< 0.005, unpaired t-test (b), one-way ANOVA (d, f). Data represent the mean ± SEM (b, d, f).

Supplementary Files

This is a list of supplementary files associated with this preprint. Click to download.

- Sourcedata.zip
- SUPPLEMENTARYMATEIRALS.docx
- SupplementaryInformationLegends.docx